THE ASTROPHYSICAL JOURNAL, 376:135–149, 1991 July 20

ANATOMY OF THE BARNARD 5 CORE

G. A. FULLER,[1] P. C. MYERS,[2] W. J. WELCH,[3] P. F. GOLDSMITH,[4] W. D. LANGER,[5] B. G. CAMPBELL,[6]
S. GUILLOTEAU,[7] AND R. W. WILSON[8]

Received 1990 October 29; accepted 1991 January 15

ABSTRACT

A study of the structure of the dense core in the dark cloud Barnard 5 (B5) and the circumstellar environment of B5 IRS 1 is presented. $C^{18}O$ and CS observations show a dense core of about 50 $M_\odot$ with a velocity gradient around the NH_3 core in B5. A map of the CO outflow from IRS 1 shows the outflow to extend in a direction nearly perpendicular to this velocity gradient. Observations of HCN with the Hat Creek Millimeter interferometer reveal three dense clumps each with mass ~ 0.1 $M_\odot$ near the young star B5 IRS 1. Two of these clumps form an elongated structure which is both perpendicular to the CO outflow from IRS 1 and parallel to the direction of the velocity gradient seen in the core material.

Subject headings: interstellar: molecules — nebulae: individual (Barnard 5) — nebulae: internal motions — nebulae: structure

1. INTRODUCTION

Studies of local molecular clouds have now identified dense, gravitationally bound regions within these clouds which have masses comparable to stellar masses. About half of these "dense cores" are currently forming low-mass stars (Beichman et al. 1984). Since these regions represent the material most intimately associated with low-mass star formation, their study is most likely to shed light on the processes involved in the final stages of cloud collapse to form stars. The dense core in B5 is one such region which is currently forming at least one low-mass star. In this paper we present new results on this dense core and the circumstellar environment of its young star. The properties of the core are described and the connection between the properties of this material and the material near the young star are discussed.

B5 is a cloud associated with an extended dust lane in Perseus, northeast of the NGC 1333 nebula at a distance of about 350 pc (Herbig & Jones 1983). The extinction appears as a filament about 1° long extending in a direction approximately 45° east of north and about 0.°5 across (Cernicharo & Bachiller 1984), corresponding to a linear size of 6×3 pc. Young et al. (1982) made several strip maps of the region in three isotopes of CO, and more recently Goldsmith, Langer, & Wilson (1986, hereafter GLW) and Langer et al. (1989, hereafter LWGB) have made more extensive CO maps of the region. The estimated total mass for the B5 cloud from the ^{13}CO measurements is about 1000 $M_\odot$. LWGB also studied the extended *IRAS* emission associated with the B5 cloud. The extinction shows a peak near $\alpha(1950) = 03^h44^m22^s.6$, $\delta(1950) = 32°42'44''$ which corresponds to the peak of the $C^{18}O$ map of GLW.

Associated with the peak extinction and the peak of the $C^{18}O$, Benson (1983) and Benson & Myers (1989) have found an ammonia core 0.46 pc in diameter with mean molecular hydrogen number density of $10^{3.8}$ cm^{-3} and mass 19 $M_\odot$. From the ammonia observations, the kinetic temperature of the gas in this core is measured to be 11 K, which is comparable to values of between 10 and 14 K determined from CO measurements (Young et al. 1982). This dense central region of the B5 cloud, traced in part by the ammonia and the $C^{18}O$ emission, will be referred to as the B5 core.

IRAS found four embedded, presumably young, stars associated with the B5 cloud core (Beichman et al. 1984). These sources range in luminosity from ~ 0.3 $L_\odot$ for IRS 4 (IRAS 03446+3254) to 9.6 $L_\odot$ for IRS 1 (IRAS 03445+3242), the most luminous and most deeply embedded object (Myers et al. 1987). GLW showed that at least three of these *IRAS* sources, including IRS 1, and possibly all four, have CO outflows. The dynamical ages for these outflows range from 10^4 yr for IRS 1 to 2.4×10^5 yr for IRS 4.

The B5 core appears to be a good example of a low-mass core which is currently forming low-luminosity stars. In this paper we will describe molecular line observations of both the B5 core and the circumstellar environment of IRS 1. The core material has been mapped in both $C^{18}O$ $J = 1 \rightarrow 0$ and CS $J = 2 \rightarrow 1$, and the region close to B5 IRS 1 has been observed in HCN $J = 1 \rightarrow 0$ using the Hat Creek Interferometer. The data for the short spacings, which were not present in the interferometer data, were obtained from a fully sampled HCN $J = 1 \rightarrow 0$ map made with the FCRAO 14 m telescope. Finally, a map of the CO outflow associated with B5 IRS 1 made with the IRAM 30 m telescope is presented.

2. OBSERVATIONS

2.1. CS *and* $C^{18}O$ *Data*

B5 has been mapped in both $C^{18}O$ $J = 1 \rightarrow 0$ (at 109.78216 GHz) and CS $J = 2 \rightarrow 1$ (at 97.98097 GHz) as part of a larger

[1] Astronomy Department and Radio Astronomy Laboratory, University of California, Berkeley; postal address: Harvard-Smithsonian Center for Astrophysics, 60 Garden Street, Cambridge, MA 02138.
[2] Harvard-Smithsonian Center for Astrophysics, 60 Garden Street, Cambridge, MA 02138.
[3] Astronomy Department and Radio Astronomy Laboratory, University of California, Berkeley; postal address: Radio Astronomy Laboratory, University of California, Berkeley, CA 94720.
[4] Five College Radio Astronomy Observatory, Lederle Research Tower B, Department of Physics and Astronomy, University of Massachusetts, Amherst, MA 01003.
[5] Princeton University, P.O. Box 451, Princeton, NJ 08543.
[6] Department of Physics and Astronomy, University of New Mexico, 800 Yale Boulevard, N.E., Albequerque, NM 87131.
[7] Institut de Radio Astronomie Millimétrique, Domaine Universitaire de Grenoble, F-38406, St. Martin d'Héres Cedex, France.
[8] HOH-L239, AT&T Bell Laboratories, Holmdel, NJ 07733.

study of the gas properties in dense cores (Fuller 1989; Fuller & Myers 1991; Myers et al. 1991). The $C^{18}O$ data were taken with the 14 m telescope at the Five College Radio Astronomy Observatory (FCRAO)[9] in 1985 December and 1988 April. The region around the NH_3 core identified by Benson (1983) was mapped with 1′ spacing close to the NH_3 core and 2′ spacing farther out. The mapping was carried out using a 100 kHz filterbank spectrometer, giving a velocity resolution of 0.27 km s^{-1}.

The CS $J = 2 \rightarrow 1$ map of B5 was made in 1986 May and October with the National Radio Astronomy Observatory[10] 12 m telescope. Once again the region close to the known NH_3 core was mapped with 1′ spacing and 2′ spacing farther out. The mapping was carried out using both polarizations of the dual channel receiver. Each polarization was fed into 128 100 kHz filters, giving a velocity resolution of 0.3 km s^{-1}. The spectra from both polarizations at each position observed were averaged together before being analyzed. Both the CS and $C^{18}O$ emission were mapped out to the boundary where the spatial half-peak contour was well defined.

2.2. HCN *Data*

The HCN data were taken between 1986 October and 1987 December using the three-element BIMA Hat Creek Millimeter Interferometer.[11] The observations used the spectral line digital correlator with two sections each of a bandwidth of 5 MHz ($\sim$17 km s^{-1}) covering 128 spectral channels in each sideband of the first local oscillator. The HCN $J = 1 \rightarrow 0$ transition (centered at 88.6318473 GHz) was observed in the lower sideband with the main hyperfine component centered in one of two correlator sections. The other correlator section was slightly offset in velocity with respect to the first section. During the data reduction, comparison of maps covering the same velocity ranges in each correlator section were found to be indistinguishable. The maps discussed here were made exclusively from spectral channels in the correlator section centered on the main hyperfine component. Typically spectra taken with a correlator are Hanning-smoothed during the observations; however, this was not done for these observations, in order to obtain a specral resolution of 39 kHz (0.13 km s^{-1}). The instrumental phase was measured about once every 20 to 30 minutes during the observations by observing the quasars 3C 84 and PKS 0420−014. The amplitude scale was calibrated by comparison of the quasar fluxes with the measured fluxes of various planets. These measurements typically gave values between 220 and 300 Jy K^{-1} for the three telescopes.

Observations of the HCN $J = 1 \rightarrow 0$ line were also made using the FCRAO 14 m telescope between 1986 May 7 and 11 and on 1986 June 4. A Nyquist-sampled map of the B5 IRS 1 region over an area comparable to the Hat Creek Interferometer primary beam was made to provide data on the large-scale structure not sampled by the interferometer observations. The data were taken at 30″ spacing over a region $\pm$1′ around B5 IRS 1, using a spectrum expander and 100 kHz filter bank to give a spectral resolution of 25 kHz (0.084 km s^{-1}), which is slightly higher than the resolution of the Hat Creek data. A total of about 12 hr was spent making this map so that the absolute noise level in the average of all the spectra in the map is comparable to that for the integrated data on one interferometer spacing. In addition to the HCN map, spectra of $H^{13}CN$ were also obtained toward IRS 1.

2.2.1. *Reduction and Combination of Data*

The interferometer data were first corrected for the instrumental phase drift. This was done by either fitting a polynomial function to the observed calibrator phases as a function of time, or using piecewise linear interpolation between calibrator observations. This smooth function or linear interpolation was used to interpolate the instrumental phase to the time of the source measurements. This phase was then subtracted from the measured phase. During the observations of the phase calibrators, the spectral line correlator mode was reset to cover 320 MHz of the IF passband in order to maximize the signal-to-noise ratio for the short, typically 5 minute, observations. Then the correlator was set back to the two 5 MHz windows as mentioned above, for the source observations. The phase offset between those spectral channels at the same sky frequency as the center of the narrow-band setup and the average phase across the whole sideband was measured and this offset was applied to the source data when it was gridded.

The Hat Creek observations of B5 IRS 1 cover a range of projected baselines from about 1.5 to 18 kλ. The uncertainty in the phase calibration leads to an estimate of the positional uncertainty in the Hat Creek maps of 1″. The estimated uncertainty in the amplitude calibration is between 20% and 30%.

The FWHM beam size of the FCRAO 14 m antenna measured during the HCN observations was 62″. During the reduction of the spectra a polynomial baseline was removed from each spectrum and the spectra stored as a three-dimensional datacube. Before being Fourier-transformed to the (u, v) plane, the spectra were scaled by a factor of 36.3 Jy K^{-1} to convert from measured antenna temperature to janskys.

The Hat Creek and FCRAO data were combined by Fourier-transforming the single-dish map to the (u, v) plane and then treating these data in a manner identical to the interferometer data. Details of the method used are given in Vogel et al. (1984) and Fuller (1989). Before combining the data the relative calibration of the Hat Creek and FCRAO data was checked by generating (u, v) data from the FCRAO map for baselines present in the interferometer data and comparing the amplitudes. This comparison was done for the region 1.5–2.6 kλ, and the relative calibration of the two data sets was within the uncertainties of each data set. The data for combination with the interferometer data was generated by Fourier-transforming the FCRAO data for a discrete set of equivalent baselines with separations of multiples of 0.54 kλ up to 2.7 kλ plus a single spacing at 0.09 kλ, but the data were truncated at baselines greater than 1.9 kλ (corresponding to about 6 m, or 22 ns).

The interferometer and transformed single-dish data were then gridded, Fourier-transformed, and CLEANed in the usual manner. The maps presented here were made with natural weighting with the single-dish data weighted so that it contributed at about the same level as one of the interferometer tracks. This leads to a beam of 12″.8 × 12″.3 with the major axis at position angle 17°.

[9] The FCRAO is operated with the support of the National Science Foundation and with the permission of the Metropolitan District Commission of the Commonwealth of Massachusetts.

[10] The National Radio Astronomy Observatory is operated by Associated Universities Inc., under contract with the National Science Foundation.

[11] The BIMA Hat Creek Interferometer is operated under a joint agreement between the University of California, Berkeley, the University of Illinois, and the University of Maryland.

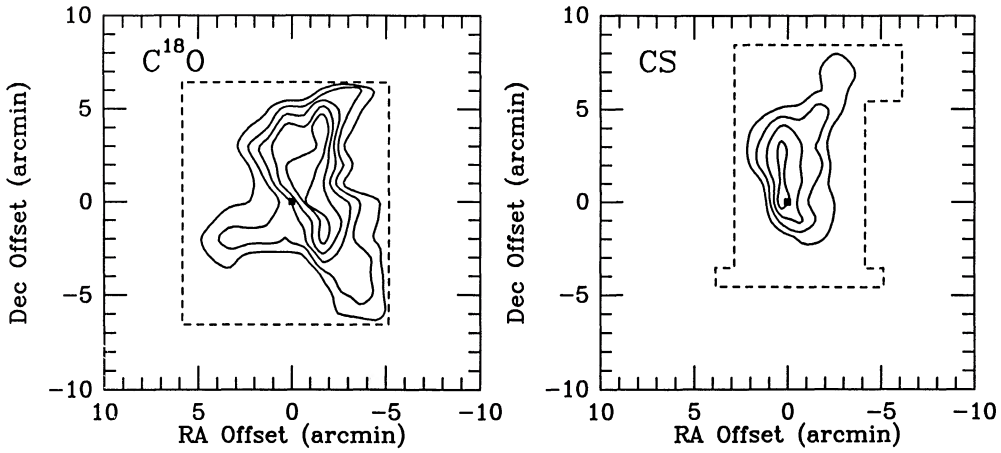

FIG. 1.—The panel to the left shows the line peak temperature (T_A^*) of the $C^{18}O$ $J = 1 \rightarrow 0$ emission of the B5 core. The contour levels start at 0.6 K and increase in steps of 0.2 K. The rms noise level in a typical spectrum is about 0.1 K. The map is centered at $\alpha(1950) = 3^h44^m31^s.8$, $\delta(1950) = 32°42'32''$, the location of the *IRAS* source IRS 1. The broken line shows the limit of the region mapped. The right panel shows the CS $J = 2 \rightarrow 1$ emission in the same region. The map is centered at the same location as the $C^{18}O$ map. The contour levels start at $T_R^* = 0.8$ K and increase in steps of 0.3 K. Again the broken line shows the limit of the region mapped. The rms noise level in a typical spectrum in the map is 0.08 K.

2.3. CO *Observations*

Observations of ^{12}CO $J = 1 \rightarrow 0$ to map the outflow from B5 IRS 1 were made with the IRAM 30 m telescope during 1987 June using the 3 mm receiver and a 256 channel 100 kHz filter bank. The typical system temperature corrected to above the atmosphere during the observations was $\sim$1400 K. The typical noise on a spectrum in the map is $\sigma(T_R^*) = 0.3$ K. The data were taken by position-switching, and no baseline was subtracted before their addition to the map. The data consisted of 105 spectra covering a region $\sim 3' \times 5'$ in extent centered on the position $\alpha(1950) = 3^h44^m32^s$, $\delta(1950) = 32°42'30''$.

3. RESULTS

3.1. CS *and* $C^{18}O$

The maps of $C^{18}O$ and CS line peak temperature, as determined from a Gaussian fit to the spectrum at each map position, are shown in Figure 1. Although the CS is somewhat smaller in extent than the $C^{18}O$, both maps show a north-south ridge of emission, as does the NH_3 map (Benson & Myers 1989). The maps also show some evidence for an extension to the northwest at the northern end of the core. In the $C^{18}O$ map, there is also a suggestion of an extension to the southwest at the southern end of the core, and thus the map has a slight overall convex appearance. Since both the CS and $C^{18}O$ maps were mapped to the half-peak contour and the CS half-peak contour closes more quickly to the south than does the $C^{18}O$ contour, the CS map does not extend far enough to the south to see whether it also shows the southwestward extension.

To provide quantitative information about the size and shape of the core, the size and shape of each map were determined from the line peak temperature data by finding where the principal axes of the distribution of emission crossed the half-peak contour. First, the location of the centroid of emission was determined and then the matrix of the second moments of the line peak temperature [$\sum T(\Delta R.A.)^2$, $\sum T(\Delta decl.)^2$, $\sum T(\Delta R.A. \Delta decl.)$] was diagonalized to determine the principal axes of the emission. The size of the core in each of the principal axis directions was then defined to be the length of the line parallel to the principal axis, passing through the centroid, contained within the half-peak contour. When a single value for the core size is given, it is the geometric mean of the sizes in the two principal axis directions. The axial ratio of the core is the ratio of the smaller to larger size in the two principal axis directions. The long axis direction gives the position angle of the core. The results for the core shapes are given in Table 1. As can be seen, the results are in good agreement with the overall visual impression both in terms of the shape and relative size of the maps. For comparison, the equivalent measurements for the ammonia map from Benson & Myers (1989) are also included in Table 1.

The CS and $C^{18}O$ are similar in their line profiles, as well as the shape and extent of their emission. Figure 2 shows the

TABLE 1

CORE PROPERTIES

TRACER	DIAMETER a (10^{18} cm)	DIAMETER b (10^{18} cm)	AXIAL RATIO	POSITION ANGLE (°E of N)	VELOCITY GRADIENT (km s^{-1} pc^{-1})	GRADIENT DIRECTION (°E of N)
$C^{18}O$	3.2	1.0	0.32	17	0.60 ± 0.02	148 ± 3
CS	2.2	1.2	0.54	−13	0.75 ± 0.03	134 ± 3
NH_3	1.7	0.47	0.3	5	0.44 ± 0.10	126 ± 11

NOTE.—a and b are the FWHM projected diameters, as explained in § 3.1.

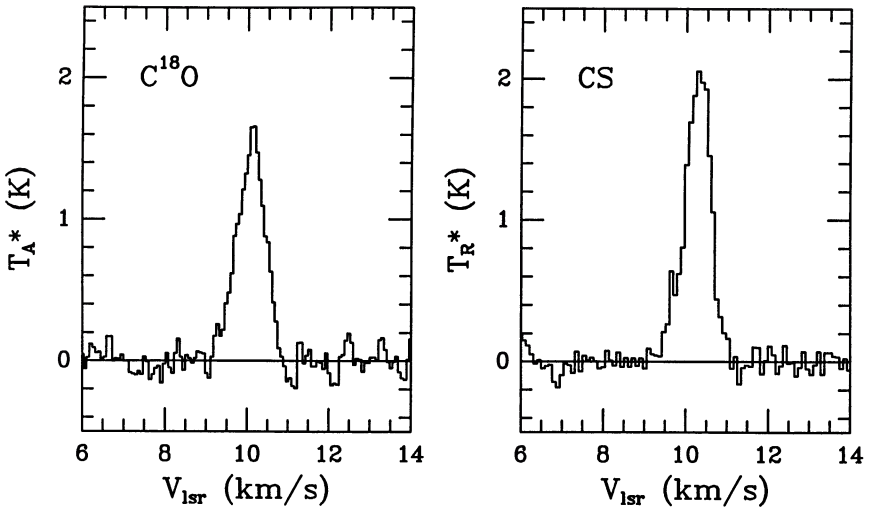

FIG. 2.—High-resolution spectra of the $C^{18}O$ $J = 1 \rightarrow 0$ (*left*) and CS $J = 2 \rightarrow 1$ (*right*) emission toward the infrared source B5 IRS 1

spectrum of the CS $J = 2 \rightarrow 1$ and $C^{18}O$ $J = 1 \rightarrow 0$ emission toward IRS 1. The peak velocity and widths of these lines are very similar. The CS has a peak velocity of 10.3 km s^{-1} and a line width of 0.8 km s^{-1}, whereas the $C^{18}O$ has a peak velocity of 10.1 km s^{-1} and a width of 0.7 km s^{-1}. Over the maps the median line centroid velocity for the $C^{18}O$ is 10.1 km s^{-1}, the same as for the CS emission. The median line widths over the maps are 0.86 and 0.92 km s^{-1} for the $C^{18}O$ and CS, respectively. Analysis of the line peak velocity (also determined from Gaussian fits to the spectra) indicates the presence of a velocity gradient across the B5 core. In both the CS and $C^{18}O$, the line peak velocities are smaller in the northwest of the core and apparently smoothly change to larger velocities in the southeast. A two-dimensional velocity fit gives the results shown in Table 1. Again it can be seen that the results for CS and $C^{18}O$ are very similar. The ammonia observations also show a velocity gradient of comparable magnitude and direction to those seen in CS and $C^{18}O$.

3.2. HCN *Data*

The $J = 1 \rightarrow 0$ transition of HCN comprises three hyperfine components, $F = 1$–1, $F = 2$–1, and $F = 0$–1. The two satellite lines lie -7.06 and $+4.84$ km s^{-1} relative to the main, $F = 2$–1, component. Figure 3 shows clearly all three hyperfine components of the HCN $J = 1 \rightarrow 0$ toward B5 IRS 1 from the FCRAO data. This figure also includes a schematic showing the positions and relative strengths of the hyperfine components in the optically thin, uniform excitation temperature limit. Clearly the intensities of the three components are not in this ratio as both the outer hyperfine lines are stronger relative to the main component. The ratio of the intensities is evidence that the lines are not optically thin, as will be discussed in more detail below. All three hyperfine components are quite narrow, with FWHM of 0.64, 0.61, and 0.65 km s^{-1} for the $F = 0 \rightarrow 1$, $F = 2 \rightarrow 1$, and $F = 1 \rightarrow 1$ components, respectively. The central velocities of the three hyperfines are all consistent with each other within 0.08 km s^{-1} (about one-eighth of the line width) and a core velocity of 10.3 km s^{-1}, consistent with the velocities of other observed molecules. The line shapes are all very similar. They appear slightly non-Gaussian with a steep decline on the high-velocity side of the line peak and a more extended wing on the low-velocity side.

In all three hyperfine components, the line-integrated maps made from the combined Hat Creek and FCRAO data show emission which peaks close to IRS 1 but which is not centered on it. In overall properties, the emission in each hyperfine line is similar, most of the emission arising from one region to the northeast of the infrared source. In all three maps, this region shows some extension in a direction close to position angle 135° (east of north).

Figure 4 shows the CLEANed maps of the main hyperfine emission averaged over two different velocity ranges. The first is centered at 10.1 km s^{-1}, and the second is centered at 10.5 km s^{-1}. Both cover 0.4 km s^{-1}. Figure 5 shows the CLEANed average emission of the two outer hyperfine components in the same two velocity ranges. The spatial resolution of these maps is 12.″8 × 12.″3 at position angle 17.°4, and the half-power beam is shown in the lower left of each map. The (0, 0) position of each map is $\alpha(1950) = 3^h44^m31^s.79$, $\delta(1950) = 32°42'32''.0$, consistent with the position of B5 IRS 1 measured at 2 μm by

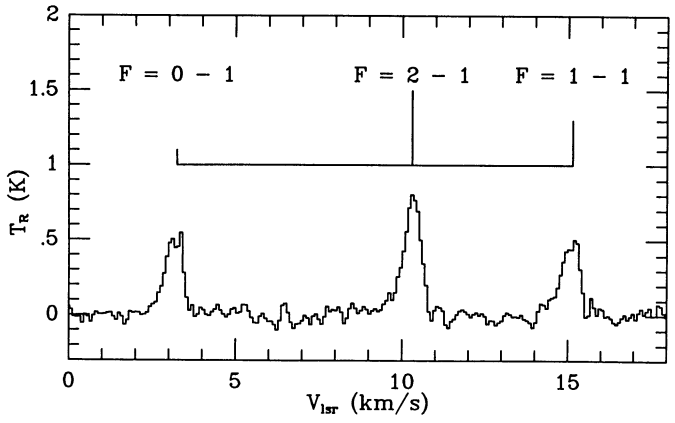

FIG. 3.—The HCN $J = 1 \rightarrow 0$ spectrum toward B5 IRS 1 from the FCRAO 14 m telescope. The three hyperfine components are clearly visible and well separated. The diagram above the spectrum shows the expected hyperfine splitting, which is very close to the observed line peak separation. The heights of the lines in the diagram show the expected line ratio if the transition is optically thin with a uniform excitation temperature. The observed line ratios are inconsistent with these ratios. The observed $F = 0 \rightarrow 1$ line is stronger than would be expected from the $F = 2 \rightarrow 1$ and $F = 1 \rightarrow 1$ components.

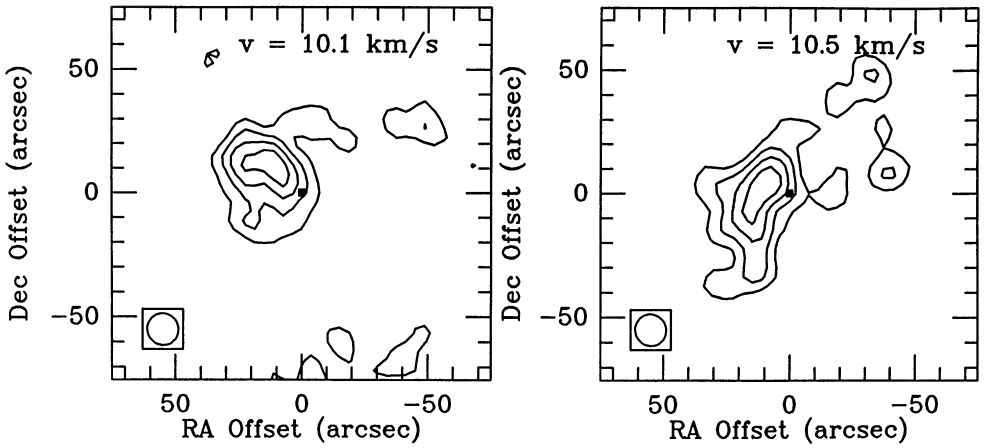

FIG. 4.—CLEANed map of HCN $J = 1 \rightarrow 0$ main hyperfine component ($F = 2 \rightarrow 1$) emission. The panel on the left shows the emission integrated over the range from 9.9 to 10.3 km s^{-1}. The right-hand panel shows the emission integrated from 10.3 to 10.7 km s^{-1}. The maps are the result of the combination of the data from the Hat Creek Interferometer and from the FCRAO 14 m telescope as described in the text. The beam is 12″.8 by 12″.3 with the major axis 17° east of north. In both figures, the square boxes the position of B5 IRS 1. The lowest contour is 0.4 K km s^{-1}, and the contours increase in steps of 0.2 K km s^{-1}.

Myers et al. (1987). Since the optical depth in the average of the outer hyperfine components (Fig. 5) is lower than that in the main hyperfine line, these maps probably trace the total column density in the region near IRS 1 better than those of the main hyperfine component.

In Figures 4 and 5, the structure seen in the integrated hyperfine maps has broken into two components, one at 10.1 km s^{-1} which extends to the northeast of IRS 1 (clump C). This clump is clearly seen in both the main and outer hyperfine components. At 10.5 km s^{-1}, there is an elongated structure which extends in a direction close to perpendicular to the direction from IRS 1 to the clump C in both figures. In the optically thinner outer hyperfine components (Fig. 5), this structure breaks up into two clumps (clumps A and B) lying on a line at a position angle close to 135° (east of north). The differences in detail between Figures 4 and 5 are probably the result of the difference in optical depth. The locations of clumps A, B, and C have been assigned on the basis of the maps of the average of the outer two hyperfine components. The positions of these clumps are given in Table 2 along with the sizes of the clumps at the half-peak contour. Table 3 gives the resulting Gaussian fits to the HCN hyperfine components averaged over each clump.

3.3. CO *Outflow*

Figure 6 shows the CO $J = 1 \rightarrow 0$ emission mapped with the IRAM 30 m telescope in two redshifted and two blueshifted velocity ranges in the line wings. The peak velocity of the CO is close to 10 km s^{-1}, which is consistent with the other molecular tracers in the B5 core. The high-velocity line wings extend from about 0 to 20 km s^{-1}. The maps show the blue- and redshifted material to be spatially separated and elongated in a direction close to 65° east of north covering the total extent of about 5′, or 0.5 pc. This is a lower limit to the size of the outflow as neither lobe has been fully mapped to the point where the line wing is no longer detectable. In the red lobe, the line wing becomes confused with the wings from the outflows

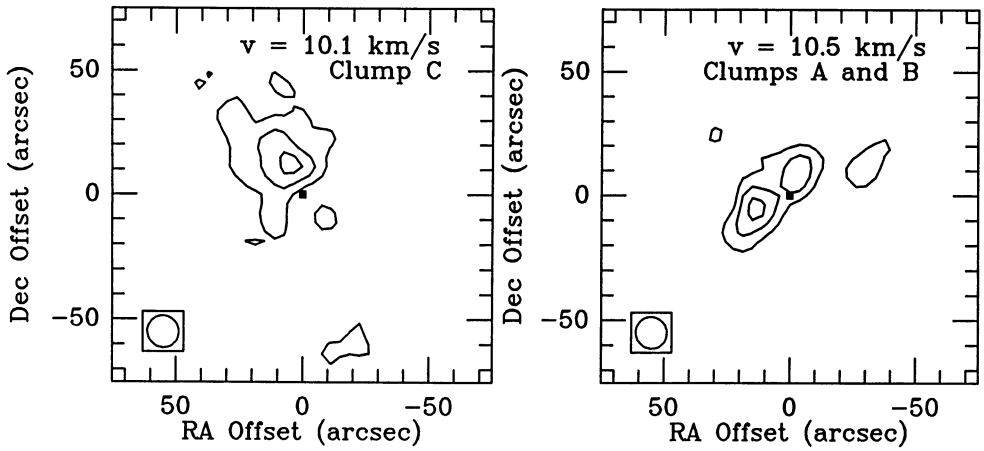

FIG. 5.—CLEANed map of the average of the $F = 0 \rightarrow 1$ and $F = 1 \rightarrow 1$ component of HCN $J = 1 \rightarrow 0$ transition. The panel on the left shows the emission integrated over the range from 9.9 to 10.3 km s^{-1}. The right-hand panel shows the emission integrated from 10.3 to 10.7 km s^{-1}. These are the same velocity ranges as shown for the main hyperfine component in Fig. 4. In both figures the square marks the position of B5 IRS 1. The lowest contour is 0.4 K km s^{-1}, and the contours increase in steps of 0.2 K km s^{-1}.

TABLE 2

HCN CLUMP PROPERTIES

Clump	Location[a] ΔX (arcsec)	Location[a] ΔY (arcsec)	Radius (10^{16} cm)	Line Width FWHM (km s^{-1})	$N(H_2)$ (10^{21} cm^{-2})	Mass ($M_\odot$)	H_2 Number Density (10^4 cm^{-3})	Virial Mass ($M_\odot$)
A	−13	−7	6.3	0.70	5.3	0.13	6.3	1.2
B	2	8	3.7	0.69	12	0.10	24	0.7
C	−11	12	8.9	0.71	6.7	0.32	5.6	1.8
All[b]	...	...	13	0.70	5.3	0.55	3.1	2.6

[a] Offset from central position R.A.(1950.0) = $3^h44^m31^s.8$, decl.(1950.0) = 32°42′32″.
[b] Measurements averaged over whole region of HCN emission near IRS 1.

associated with B5 IRS 2 and IRS 3 (GLW). The outflow is rather well collimated with the ratio of axial to lateral extent of just over 3:1. The red lobe is significantly more extended than the blue lobe, extending out about 1.5 times further than the blue lobe.

In both the red and blue line wing maps, the outflow appears to be dominated by a single peak of emission in the velocity ranges closest to the line core, but at more extreme velocities the emission breaks up into several clumps. Analysis of the maps made in 2 km s^{-1} velocity bins suggests that in the blue wing in the velocity range 4 to 8 km s^{-1}, the peak of the emission occurs at increasing distance from B5 IRS 1 with increasing velocity difference from the line center. To investigate this behavior in a more systematic manner, the emission-weighted size as a function of velocity, $R(v)$, of the outflow was examined where

$$R(\bar{v}_i) = \frac{\sum_{x,y} \sum_{v=\bar{v}_i-\Delta v/2}^{\bar{v}_i+\Delta v/2} r(x, y) T_R^*(v) \Delta v}{\sum_{x,y} \sum_{v=\bar{v}_i-\Delta v/2}^{\bar{v}_i+\Delta v/2} T_R^*(v) \Delta v},$$

and $r(x, y) = (x^2 + y^2)^{1/2}$ is the distance of the pixel at (x, y) from the map center, $\bar{v}_i$ and Δv are the mean velocity in velocity range i and the width of the velocity bins, respectively. This statistic is similar to that defined and used by Goldsmith et al. (1984) to examine how the size of outflows varies with velocity. For the B5 data the statistic $R(v)$ was calculated for 1 km s^{-1} bins. The values derived varied from 1.′0 to 1.′8 with statistical uncertainties between 0.′01 and 0.′3. Within these uncertainties, there was no evidence for any systematic trend of size with velocity. The results are consistent with a velocity independent distribution of material in the outflow. This behavior is similar to the results for the objects mapped by Goldsmith et al. (1984) who also concluded that the spatial distribution of high-velocity gas is independent of velocity.

The energetics of the outflow have been calculated assuming that the CO is optically thin and has a 10 K excitation temperature (Goldsmith et al. 1984). Since it is likely that the optical depth, at least in the inner parts of the line wing, is considerably higher than unity and that the excitation temperature is higher than 10 K, the column densities, masses, energies, and momenta quoted for the outflow are all lower limits to their true values. Since the inclination to the line of sight is also uncertain, this correction has also not been made. The outflow properties were calculated for 1 km s^{-1} bins in the range of velocities covered by the outflow gas, 0–9 km s^{-1} for the blue wing and 11 to 20 km s^{-1} for the red wing. In each velocity bin, only pixels where the line-integrated intensity exceeded the estimated noise, 0.2 K km s^{-1}, in that bin were included. The estimates are corrected for the incomplete sampling by dividing the calculated value for each velocity range by 0.6, the estimated fraction of the outflow area actually sampled by the observations.

The total mass in the outflow in the velocity range 0–9 km s^{-1} and 11–20 km s^{-1} is 0.3 $M_\odot$. From the observed line velocity, the total momentum is 0.54 $M_\odot$ km s^{-1}, and the energy in the outflow is 2.7×10^{43} ergs. Except for the mass, these values are consistent with those derived by GLW from a lower resolution map of this outflow. The larger mass derived here is believed to arise from the inclusion of material at velocities closer to the cloud systemic velocity than considered by GLW. Adopting a mean velocity of the outflow of 5 km s^{-1}, and a typical emission-weighted size of 1.′6 leads to an estimate of a dynamical age for the outflow of 3×10^4 yr.

TABLE 3

GAUSSIAN FITS TO HCN SPECTRA AVERAGED OVER CLUMPS

Clump	Hyperfine Component	T_R (K)	FWHM (km s^{-1})	V_{lsr} (km s^{-1})	σ (K)
A	0–1	1.15	0.70	3.10	0.09
	1–1	1.62	0.44	15.13	0.15
	2–1	2.82	0.48	10.34	0.14
B	0–1	2.25	0.69	3.21	0.3
	1–1	2.35	0.43	15.08	0.4
	2–1	2.28	0.58	10.32	0.3
C	0–1	1.38	0.71	3.11	0.2
	1–1	1.43	0.48	15.0	0.1
	2–1	1.79	0.71	10.28	0.2

4. ANALYSIS

4.1. $C^{18}O$ *and* CS

During the $C^{18}O$ observations, a spectrum of the ^{13}CO $J = 1 \rightarrow 0$ transition toward IRS 1 was obtained which can be used to estimate the optical depth in the $C^{18}O$ line. The method used to derive the $C^{18}O$ optical depth is that described in detail by Myers, Linke, & Benson (1983). This method makes three basic assumptions which appear all to be approximately true for the ^{13}CO and $C^{18}O$ emission in B5. These assumptions are (1) the excitation temperature should be the same for both isotopes, (2) the beam-filling factors are the same for both isotopes, and (3) the velocity gradient (approximated as the ratio of line width to size of the emission region) is the same for both isotopes. Under these assumptions, this method gives a value of 0.46 for the optical depth of

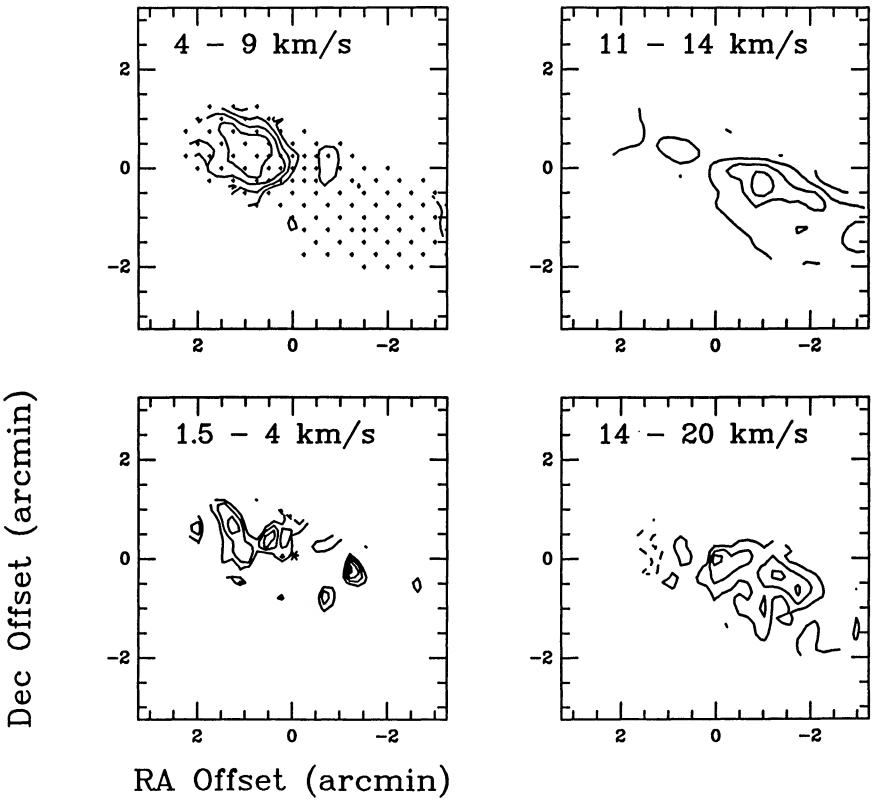

FIG. 6.—The four panels show the CO outflow from B5 IRS 1 mapped with the IRAM 30 m telescope. The panels show four different velocity ranges in the line wings. The lower panels show the most extreme line wings, and the upper panels, the material closer to the cloud LSR velocity (~ 10 km s^{-1}). The blueshifted material is shown in the two panels to the left. The lower panel shows the emission integrated from 1.5 to 4 km s^{-1}. The lowest contour level is 0.5 K km s^{-1}, and the contour spacing is 0.2 K km s^{-1}. The upper figure shows the CO emission integrated from 4 to 9 km s^{-1}. The lowest contour level is 2 K km s^{-1}, and the contour spacing is 2 K km s^{-1}. The two panels on the right show the redshifted emission. The lower panel shows the emission integrated from 14 to 20 km s^{-1}. The lowest contour level is 1 K km s^{-1} and the contour spacing is 1 K km s^{-1}. The broken contour indicates emission with integrated intensity of -1 K km s^{-1}. This arises from baseline uncertainties in a few spectra. The upper right figure shows the CO emission integrated from 11 to 14 km s^{-1}. The lowest contour level is 4 K km s^{-1} and the contour spacing is 4 K km s^{-1}. The grid of positions at which observations were taken is indicated by the small crosses on the upper left figure. The maps are centered at $\alpha(1950) = 3^h44^m32^s$, $\delta(1950) = 32°42'30''$ and the star in the lower left panel indicates the position of B5 IRS 1.

the $C^{18}O$ line toward IRS 1, a value which is in good agreement with the value of 0.4 obtained by Myers et al. (1983) at a slightly different position in B5 observed with a beam of about twice the size used in this work.

Using an excitation temperature of 10.3 K, derived from the observed strength of the $C^{18}O$ line plus a line peak optical depth of 0.46, the total $C^{18}O$ column density toward IRS 1 is 2.6×10^{15} cm^{-2}. Using the relationship

$$N(C^{18}O) = 3.4 \times 10^{14} A_v \text{ cm}^{-2} ,$$

from Bachiller & Cernicharo (1986) plus $N(H_2) = 0.94 \times 10^{21} A_v$ cm^{-2} (Bohlin, Savage, & Drake 1978) gives a total H_2 beam averaged column density of 7.2×10^{21} cm^{-2} toward IRS 1. The correlation between A_v and $C^{18}O$ column density found by LWGB leads to a column density lower by about 16%. The mean $C^{18}O$ column density across the map of the B5 core is 2.3×10^{15} cm^{-2}, assuming an excitation temperature of 10 K. Multiplying the mean H_2 column density across the map by the half-peak area of the $C^{18}O$ map gives a total mass of 51 $M_\odot$. This mass corresponds to a volume-averaged number density of 4300 cm^{-3} if the core is assumed to be a sphere with projected area equal to the observed area of the core. This value of the density is somewhat larger than the 3000 cm^{-3} derived by Wilson, Langer, & Goldsmith (1981) from observations of the $J = 2 \rightarrow 1$ and $J = 1 \rightarrow 0$ transitions of $C^{18}O$.

Although the CS emission from B5 is very similar is extent and shape to the $C^{18}O$, Zhou et al. (1989) derived a density for the CS-emitting region of 4×10^4 cm^{-3}, 10 times higher than the density derived from the $C^{18}O$ emission. The derived CS density is also about 6 times higher than the density derived from the ammonia emission, even though the ammonia comes from a much smaller region. Therefore it appears that both the size and density derived from the ammonia and $C^{18}O$ observations are consistent with a model in which the gas in the core is centrally condensed, with a single local maximum, whereas the CS emission is not. Zhou et al. (1989) have attributed the CS emission to dense clumps of material within the core. However, models comprising an envelope around a single dense central region also appear to explain a number of features of the CS emission, especially the large spatial extent of the CS emission (Fuller 1989; Fuller & Myers 1991). Owing to the uncertainty in how the CS emission arises, the CS map cannot be straightforwardly used to derive the properties of the material in the B5 core such as mass or column density. The relevance of clumpy models for the B5 core will be discussed later.

4.2. HCN

The abundance of a molecular constituent observed in emission is best determined if its optical depth is small. The spectra of the three hyperfine components of HCN shown in Fig. 3

indicate that this emission is not optically thin, so that it will not easily yield an accurate abundance. On the other hand, the relatively rare $H^{13}CN$, which we have also observed, is not optically thick, and we can readily derive its column density toward B5 IRS 1. From that column density and a known ratio of $H^{12}CN/H^{13}CN$, we can then infer the $H^{12}CN$ column density.

As is usually done, we assume that HCN isotope abundance ratio is equal to the carbon isotope abundance ratio. Many authors have studied the local abundance ratio of ^{12}C to ^{13}C and derive values in the range 75 ± 8 (Wilson et al. 1981) to 43 ± 4 (Hawkins & Jura 1987). We adopt a value of 55, consistent with the work of Wannier, Penzias, & Jenkins (1982) and the more recent work by Langer & Penzias (1990). We show below that this derived abundance is also consistent with a comparison of the $H^{12}CN$ hyperfine strengths modeled by means of Monte Carlo radiative transfer methods. However, theoretical studies have shown that trace species, such as HCN, could have isotopic ratios very different from the carbon isotopic abundance ratio (Langer & Graedel 1989).

4.2.1. *Optical Depth*

In the FCRAO spectra toward B5 IRS 1, the peak antenna temperature of the main hyperfine ($F = 2 \rightarrow 1$) component of the $H^{12}CN$ is 0.75 K, while the $H^{13}CN$ has a peak temperature of 0.1 K. Assuming that the average excitation temperatures of the two species are the same and that the relative abundance is 55 leads to an optical depth of 0.14 at the peak of the $H^{13}CN$ line and 7.7 at the peak of the $H^{12}CN$ line. In view of the signal-to-noise ratio of the measurements, the uncertainty of the isotopic ratio, and the uncertainty in the assumption that the excitation temperatures are the same, we estimate that the $H^{12}CN$ optical depth could be in the range 4–10.

4.2.2. *Abundance of* HCN

From the $C^{18}O$ data and the $H^{13}CN$ spectrum measured here, it is possible to estimate the HCN abundance. Using the $H^{13}CN$ optical depth in the equation of radiative transfer with the observed line temperature (and assuming a telescope efficiency of 0.7) allows the beam-averaged excitation temperature to be calculated. The derived excitation temperature is 4.0 K. This leads to a total $H^{13}CN$ column density of 3.7×10^{11} cm^{-2}. Using the total H_2 column density derived above leads to

$$N(H^{13}CN)/N(H_2) = 5.1 \times 10^{-11} .$$

With the assumption that the HCN and H_2 derived from the $C^{18}O$ observations are distributed in the same manner along the line of sight, this value is also the fractional abundance of the $H^{13}CN$. Scaling by the adopted ratio of $H^{12}CN$ to $H^{13}CN$ of 55, this gives a fractional abundance of 2.8×10^{-9} for $H^{12}CN$ to molecular hydrogen. However the HCN abundance is uncertain by a factor 2–3 since HCN emission appears to arise from a smaller region than the $C^{18}O$ emission.

The abundance of the 13 isotope is comparable to the value of 7.5×10^{-11} measured for the average $H^{13}CN$ fractional abundance by Swade (1989) at three positions in the dark cloud L134N. But this value is significantly lower than the value of between 1×10^{-10} and 5×10^{-10} for TMC-1 derived from the observations of Irvine & Schloerb (1984) and Irvine, Goldsmith, & Hjalmarson (1987).

4.2.3. *A Comparison of the* $H^{12}CN$ *Hyperfine Line Strengths*

A second estimate of the optical depth can, in principle, be made from the ratio of the intensity of the three hyperfine components of the HCN line. By analogy with the method used above for determination of optical depth from two species, the ratio of peak intensity of the hyperfine components can be written

$$R_{12} = \frac{1 - e^{-3\tau}}{1 - e^{-5\tau}}$$

and

$$R_{02} = \frac{1 - e^{-\tau}}{1 - e^{-5\tau}},$$

where R_{02} is the ratio of the peak line temperature in the $J = 1 \rightarrow 0$, $F = 0 \rightarrow 1$ hyperfine component to the $J = 1 \rightarrow 0$, $F = 2 \rightarrow 1$ hyperfine component and R_{12}, the ratio for the $J = 1 \rightarrow 0$, $F = 1 \rightarrow 1$ component to the $J = 1 \rightarrow 0$, $F = 2 \rightarrow 1$ component and τ is the peak optical depth of the $J = 1 \rightarrow 0$, $F = 0 \rightarrow 1$ transition. In deriving these equations it has been assumed that the excitation temperatures of these levels are the same so that the ratio of optical depths is just the ratio of their degeneracies, 5:3:1 for $F = 2 \rightarrow 1 : 1 \rightarrow 1 : 0 \rightarrow 1$. Examination of Table 3 and Figure 3 shows that the observed values of the line ratios are not consistent with the line ratios from LTE excitation at a uniform temperature, but all the values suggest that the lines have significant optical depth, consistent with the measurement of the $H^{13}CN$ emission discussed above. The inconsistency with a uniform excitation temperature has been previously noted in warm, massive clouds associated with H II regions (Gottlieb et al. 1975; Guilloteau & Baudry 1981) and dark clouds (Walmsley et al. 1982). However, there seems to be a fairly straightforward explanation for the observed line ratios.

The three hyperfine components of HCN have different optical depths, and the temperature seen at line center depends upon the excitation temperature at the region in the cloud where the line optical depth, measured from the cloud surface inward, is of order unity. If there is an excitation temperature gradient in the cloud, the three lines will reflect the different excitation temperatures in their peak temperatures. In particular, if the excitation temperature in the cloud rises toward the cloud center as a result of, say, increasing density, then the optically thinest line, the $F = 0 \rightarrow 1$ component, will reflect the higher excitation temperature deeper in the cloud. The line will therefore appear to be stronger than it should be when the line temperature is compared with the other hyperfine components which become optically thick further out in the cloud in a region of lower excitation temperature. This is a possible explanation for the situation seen in B5, where the $F = 0 \rightarrow 1$ hyperfine is too strong given the strength of two other hyperfine components.

A simple single-density model is inappropriate for the density structure of a dense core. The $C^{18}O$ and CS maps clearly show that the central region of the B5 cloud containing IRS 1 is surrounded by a lower density envelope traced by $C^{18}O$, and indeed the maps of LWGB show even more tenuous material on the still larger scale. If HCN is present in this more tenuous gas, it can effect the emission seen from the core (Cernicharo et al. 1984).

In order to assess the effect of the foreground gas, the opacity of that HCN associated with the gas traced by the $C^{18}O$ will be estimated. We assume that the core "envelope" contains half the column density between the observer and IRS 1, or 3.6×10^{21} cm^{-2}, based on the FCRAO observations of

$C^{18}O$ described above. To estimate the optical depth in the HCN, a value for the excitation temperature is needed. Since the density of the gas traced by the $C^{18}O$ is between 3×10^3 cm^{-3} and 1×10^4 cm^{-3}, which is close to two orders of magnitude below the critical density for HCN $J = 1 \rightarrow 0$, the HCN will be very subthermally excited. From the $C^{18}O$ map of B5, the path length through this gas is $\sim 10^{18}$ cm. Using these parameters, the optical depth in the main hyperfine component through the envelope is ~ 1–5 for excitation temperatures between 3 and 5 K, adopting a line width in the envelope of 0.9 km s^{-1}. Clearly the HCN in the envelope has a significant effect on the emission observed. However, it is obvious that this is a crude estimate of the effect of the envelope. To make a better estimate of the role of the envelope on the radiative transfer and indeed to check on the consistency of the values derived above, the emission from B5 has been modeled using a radiative transfer computer code.

4.2.4. *Monte Carlo Models*

We used the Monte Carlo computer code of Bernes (1979) to calculate the radiative transfer through a two-component spherical cloud. This code and type of model are described in Fuller (1989) where it was used for modeling CS emission. The levels up to $J = 6$ (89 K above the ground state) were included in the calculation. The Monte Carlo models are specified by the density, kinetic temperature, and velocity width at each radius plus the fractional abundance for the species. A uniform kinetic temperature of 10 K and a two-component density and velocity width structure were used. The physical parameters of the models were chosen to approximate the observed properties of the material traced by the $C^{18}O$ and the HCN. The aim of the modeling was to attempt to match approximately the observed hyperfine line strengths and line ratios. A range of models with various physical parameters consistent with the observations was run and the parameters varied to estimate the effect of the parameters on the observed lines and to obtain a reasonable fit to the HCN observations.

The HCN was treated as a simple linear molecule, with each J level $2J + 1$ degenerate. For each model, the Monte Carlo code was run to calculate the excitation temperature of each J level in each radius shell. The population of each hyperfine level was then calculated by dividing the total population in that J level between the hyperfine components in proportion to their statistical weights. Doing this makes the assumption that the excitation temperature of each hyperfine level is the same and equal to the excitation temperature of the J level in the simple linear molecule approximation. The emission in each of the three $J = 1 \rightarrow 0$ hyperfine components was then calculated by integrating the line source function using these populations. The collision excitation rates for HCN with H_2 were found by taking the results from Green & Thaddeus (1974) for HCN with He and scaling by 50% to account for the mass difference between He and H_2. The results of Green & Thaddeus are in reasonable agreement with the more recent work of Monteiro & Stutzki (1986).

A series of these two-component models was run. Each model comprised from three to five different simulations for the same physical conditions but slightly different starting states and a different random number sequence in order to test the convergence of the models. The final level populations from these different runs were averaged and then used to calculate the line profiles. The series of models ranged in central density from 3×10^5 to 1×10^5 cm^{-3} and 1×10^4 to 1×10^3 for the outer density, with the outer radius of the low-density envelope varying between 10^{18} and 10^{17} cm. In addition several values in the range (1×10^{-9})–(5×10^{-9}) were used for the abundance of HCN relative to the mean particle density. In all the models the gas kinetic temperature was 10 K in both density regions, and velocity dispersions were 0.21 and 0.42 km s^{-1} in the high- and low-density regions, respectively. The density and HCN abundance were varied to attempt to match the observed hyperfine line peak temperatures and the peak temperature ratios. We estimate the uncertainty in the line temperatures from the models to be no greater than about 0.4 K.

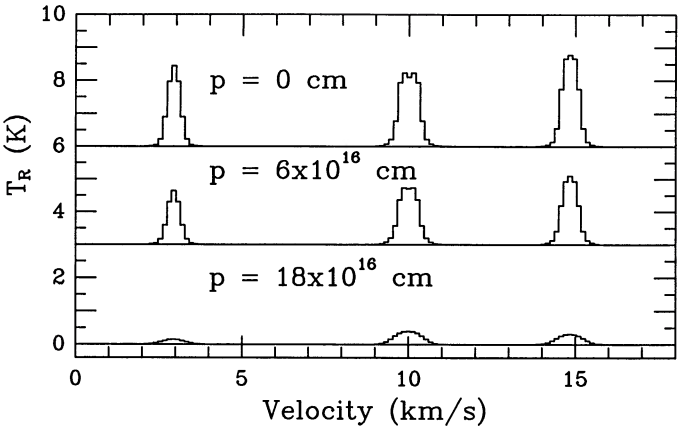

FIG. 7.—The HCN $J = 1 \rightarrow 0$ hyperfine line profiles from the best-fit Monte Carlo model. The model has a central number density of 10^5 cm^{-3} with an envelope of density 3×10^3 cm^{-3} and a kinetic temperature of 10 K. The figure shows the lines at three different impact parameters, 0 cm (*upper spectrum*), 6×10^{16} cm (*middle spectrum*), and 18×10^{16} cm (*lower spectrum*). Each line of spectra is offset by 3 K from the baseline of the spectrum below.

The line profiles from the model which most closely reproduces the observations are shown in Figure 7. The model comprised a central region of H_2 density 10^5 cm^{-3}, radius 6.2×10^{16}, and an envelope 5×10^{17} cm in radius with H_2 density 3×10^3 cm^{-3}. The HCN fractional abundance was 2×10^{-9}. Comparing this figure with the values given in Table 2 for the observed hyperfine parameters toward the HCN clumps shows that this model closely reproduces both the absolute intensities and the relative intensities of the hyperfine components. Although the model predicts that the main hyperfine component has a slight self-absorption due to the foreground material, the depth of this predicted self-absorption is smaller than the noise in the observations.

There are two regimes for the excitation temperature in the model. In the central, dense region the upper level is nearly thermalized but in the outer, low-density region the excitation temperature is much lower. However, all three hyperfine components have nearly the same peak temperature, between 2.2 K and 2.6 K, despite the fact that the excitation temperature is ~ 8 K in the central region. The relative line intensities are not the result of either beam dilution or low excitation temperature in low-density gas, but rather the combined effects of varying excitation temperature and optical depth. The hyperfine components have peak optical depths (in the central 0.13 km s^{-1} bin) of 1.2, 3.5 and 5.9 for the 0–1, 1–1, and 2–1 components, respectively. The observed line profiles are thus the result of the two thinner components sampling regions deeper in the cloud where the excitation temperature is higher than the region which the more optically thick main component probes. In the

absence of the envelope, the lines would have peak temperatures close to 7 K, so although the envelope around the central core is reducing the strength of the lines, a comparison between the line profiles seen at different project radii (see Fig. 7) shows that the core is still visible through the envelope. Note that the model optical depth of the main ($F = 2 \rightarrow 1$) hyperfine component is in good agreement with the value of 8 inferred from the $H^{13}CN$ observation as is the $H^{12}CN$ fractional abundance of 2×10^{-9}.

The $F = 0 \rightarrow 1$ component, the optically thinnest component, arises almost exclusively from the central core region. If the density in the central region is decreased by a factor of 2, then this line drops in intensity by a factor of 0.6, as its peak optical depth drops to 0.86. As a result of this change in density the peak temperature of the $F = 1 \rightarrow 1$ line drops by only a factor 0.76 and the $F = 2 \rightarrow 1$ drops to 0.86 of its previous value, considerably less than the change in the $F = 0 \rightarrow 1$ component.

In summary, these Monte Carlo models are reasonably successful in matching aspects of the observed HCN spectra, in particular the relative line strengths among the hyperfine components and the absolute line strengths. It should be remembered, however, that these Monte Carlo models contain a number of approximations and assumptions, and so the results should not be over interpreted. Nonetheless, the models show that the low-density envelope has a significant effect on the observed line profiles of the $J = 1 \rightarrow 0$ HCN transition and in attempting to derive the properties of core material from HCN observations the structure and role of the foreground must in general be considered. However, in the case of these B5 observations, the values derived from considering only the optically thinnest hyperfine component, the $F = 0 \rightarrow 1$ component, appear reasonably consistent with the Monte Carlo models and the other known properties of the core.

4.2.5. *Column Densities of Individual Clumps*

The individual clumps were mapped only in the $H^{12}CN$, and therefore their column densities must be estimated in this molecule. From the discussion above of the whole central core, we expect the $F = 0 \rightarrow 1$ hyperfine component to have an optical depth of no more than about 1. Using the observed brightness temperature in this transition and the excitation temperature derived from the Monte Carlo model of the overall core, we obtain the HCN column densities. The value obtained above for the HCN to H_2 abundance ratio can be used to convert this to the total H_2 column density. Table 2 gives the derived column density and mass, from the clump area times the column density, for the clumps near B5 IRS 1. This table also includes the clump virial masses derived from the widths of the line when averaged over the clump area.

The optical depth of the $F = 0 \rightarrow 1$ hyperfine component derived from the observed brightness temperature and the excitation temperature from the Monte Carlo models is in the range 0.2–0.8 for the three HCN clumps. These optical depths are somewhat lower than the 1–1.2 expected on the basis of the main, $F = 2 \rightarrow 1$, component optical depth derived from the comparison of the $H^{12}CN$ and $H^{13}CN$ isotopes. If the higher values of the optical depths are used, the mass of the clumps increase by a factor in the range of 1.5–2, depending on the clump, and the excitation derived for the different clumps would be in the range 5–7 K.

5. DISCUSSION

5.1. *Morphology*

As discussed earlier, the B5 cloud appears as a filament of extinction in optical photographs extending from the southwest to the northeast with a very opaque ($A_v > 6$) region elongated north-south near $3^h44^m22^s6$, 32°42′44″ (Cernicharo & Bachiller 1984). This region of high extinction is the location of the NH_3 core mapped by Benson (1983) and Benson & Myers (1989) and the $C^{18}O$ and CS core mapped in this work.

The similarity of the core in CS and $C^{18}O$ has been discussed earlier. The CS and $C^{18}O$ maps also show evidence for elongation in a roughly north-south direction. The NH_3 map of this region (Benson & Myers 1989) has a number of striking similarities with the maps presented here. Like the CS and $C^{18}O$, the NH_3 map is elongated in a roughly north-south direction (see Table 1) and has a similar axial ratio, 0.4, compared to 0.32 and 0.54 for the $C^{18}O$ and CS, respectively. The ammonia emission, however, seems to show the presence of two peaks in the north-south ridge which are not obviously apparent in the other maps. Also the ammonia has a somewhat smaller spatial extent than either of the other two molecules, which is consistent with it tracing a somewhat higher density region interior to the lower density material traced by the other molecules. Thus the B5 core is typical in its elongation, and the agreement among the CS, $C^{18}O$, and NH_3 maps, of the 16 cores compared by Myers et al. (1991).

On the larger scale the ^{13}CO maps of this region by LWGB show much more extended emission, although the position of the peak integrated intensity is close to the position of the peak of the $C^{18}O$ core. The highest levels of the ^{13}CO emission trace a structure which seems to show an extension north-south approximately aligned with the core region of the cloud, but the overall impression is of a northeast-southwest elongation of the cloud. The ^{12}CO emission, which is even more extended than the ^{13}CO, is elongated, with an axial ratio of about 0.5, in the direction northeast to southwest. This direction is similar to the direction of the CO outflow from B5 IRS 1. The ^{12}CO shows little evidence for the north-south extension of the core.

In addition to the molecular line maps of this cloud and dense core, Pendleton et al. (1990) have presented submillimeter continuum maps at 160 and 360 μm of B5. The overall appearance of both submillimeter continuum maps is a north-south elongation. The 360 μm map is the more extended of the two submillimeter maps and shows several peaks. One of these peaks is centered on B5 IRS 1, and this clump also appears in the 160 μm map. The northern peak, which is not well mapped even at 360 μm, was not covered in the region mapped at 160 μm. The southwest peak is much weaker with respect to B5 IRS 1 at 160 μm than at 360 μm. This is probably the result of lower dust temperature in the SW clump (Pendleton et al. 1990). Apart from the overall shape, the 360 μm map and the CS map have several similar features: there is some evidence in the CS map for extensions in both the NW and SW directions, and the CS follows the plateau of 360 μm emission to the north of IRS 1. However, the similarities between the $C^{18}O$ and the 360 micron maps are even stronger. The $C^{18}O$ and the 360 μm maps both have a suggestion of a convex shape and a peak near IRS 1, and although the $C^{18}O$ peak does not appear directly toward IRS 1, it is only offset by $\sim 1'$. The $C^{18}O$ map also shows some evidence for both the SW and NW 360 μm peaks. As Table 4 shows, the total mass

TABLE 4

SUMMARY OF PROPERTIES OF B5 CORE

Tracer	Radius (10^{17} cm)	Mass ($M_\odot$)	U (10^{44} ergs)
^{12}CO	52	1350–2510	560–1930
^{13}CO	43	930	320
$C^{18}O$	30	500	130
360 μm	13.5	50	3.0
$C^{18}O$	11.5	51	3.6
CS	8	40	3.2
160 μm	7.7	...	...
NH_3	5.5	8.5–19	0.2–1.0
HCN	1.3	2.6	0.08

NOTE.—Data from LWGB, Pendleton et al. 1990, Benson & Myers 1989, and this work. The range of mass for the ^{12}CO reflects the uncertainties discussed in LWGB. For the ammonia data, the smaller value is the mass estimated for the ammonia associated with B5 IRS 1 alone, while the larger value corresponds to the mass of all the ammonia in the core.

derived from the $C^{18}O$ and 360 μm maps are in remarkable agreement.

On the other hand, the 160 μm emission appears more similar in shape and extent to that of the NH_3. Both show the clump of material associated with IRS 1 and an extension to the north. In the ammonia emission, the northern extension is in fact a second clump, but in the continuum emission it appears as a plateau.

Moving from the core material to the environment closer to B5 IRS 1, Figure 8 summarizes the data from the HCN observations, the CO outflow, and a CCD image of the region from Heyer et al. (1990).[12] The CCD image is presented in a gray scale with the darkest gray representing the regions of brightest emission. In this image, the extinction from the core material can be seen from the lack of diffuse background emission over most of the image as compared to the most southerly one-sixth of the frame. In the region of the extinction, there is an arc-shaped region of emission with the apex of the arc near the center of the cloud and opening to the east. The apex of this arc lies close to the position of B5 IRS 1 (marked by a cross in the figure). The arc can be traced out to about 1′ from the apex of the emission. At low levels, the emission is reasonably symmetric, but the brightest emission is confined to the northern half of the arc. Within the arc, close to the imagined focus of the parabola, there is a pointlike knot of emission. This feature has been observed in CCD images of this region at three differ-

[12] The alignment of this CCD frame with respect to the near infrared source B5 IRS 1 presented in Fig. 1 of Heyer et al. (1990) is incorrect. The true location of B5 IRS 1 with respect to the optical emission arc is as shown in Fig. 8.

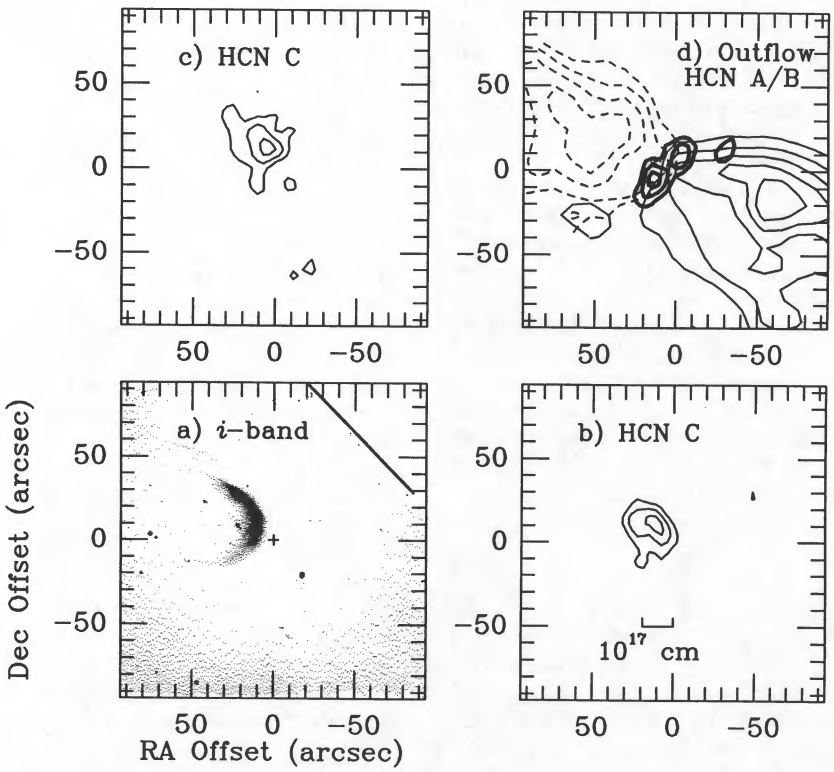

FIG. 8.—Each panel in this figure is centered at the same location, $3^h44^m31^s.8$, 32°42′32″, and the 2 μm location of B5 IRS 1 is marked by a cross on the lower left panel. (*a*) This panel shows a gray scale of the *i*-band ccd of the region near B5 IRS 1 (Heyer et al. 1990). The diagonal line in the upper left of the frame is an artifact in the image. Notice that the upper half of the arc is the brightest (darkest gray scale) portion of the arc. (*b*) and (*c*). These show the HCN clump C in the main hyperfine component (*b*) and the average of the outer hyperfine components (*c*). In each map the lines have been integrated over the same velocity range as in Fig. 4. This clump is located very close to the brightest region of the emission arc in the ccd frame. The bar in panel *b* indicates a length of 10^{17} cm assuming a distance to B5 of 350 pc. (*d*) This panel shows the HCN elongated structure formed by clumps A and B in the average of the outer hyperfine components (as shown in Fig. 5) with the redshifted (*solid contours*) and blueshifted (*broken contours*) CO outflow emission. The red line wing has been integrated over the velocity range from 11 to 20 km s^{-1}, and the contour levels start at 7 K km s^{-1} and increase in steps of 3 K km s^{-1}. The blue line wing has been integrated over the range 0 to 9 km s^{-1}, and the lowest contour is at 4 K km s^{-1} and the contour interval is 2 K km s^{-1}. The elongated HCN structure is close to perpendicular to the axis of the CO outflow and nearly tangent to the emission arc seen in the CCD frame.

ent epochs and has a measured proper motion of 0".3 yr^{-1} in the direction 70° east of north. This knot of emission appears to be moving in a direction close to parallel to the axis of the CO outflow and perpendicular to the structure formed by HCN clumps A and B.

Comparing the CCD image with the map of the integrated CO line wings shows the emission arc corresponds very closely to the outer edge of the blue wing of the CO outflow. A similar parabolic-shaped region of high surface brightness with its apex near the infrared source responsible for a CO outflow is seen in the core L43 (Mathieu et al. 1988). The northern, bright region of the arc also closely coincides with HCN clump C (shown in Fig. 8 in both the main hyperfine component and the average of the outer hyperfine components). It appears that HCN clump C may be an extension toward IRS 1 of the clump in the blue outflow wing which forms the peak of the blue-shifted emission. A peak of bright emission is seen in a similar location in the FCRAO HCN maps of the outer hyperfine components. As well as the spatial coincidence of this clump and the blue outflow wing, clump C is also at a slightly blue-shifted velocity compared to other HCN emission, 10.1 km s^{-1} compared to either 10.3 km s^{-1}, the centroid of the single spectra, or 10.5 km s^{-1} for clumps A and B.

On the other hand, the elongated structure formed by HCN clumps A and B seem to lie along a tangent to the edge of the arc of emission and close to perpendicular to the axis of the CO outflow. The direction of elongation of clumps A and B is also perpendicular to the average orientation of the optical polarization of vectors of background stars seen through the molecular cloud (Joshi et al. 1985) which is 45° east of north. The optical polarization is thought to be caused by dust grains aligned by the cloud magnetic field with the field direction being parallel to the polarization vectors.

To summarize, the three HCN clumps appear to be related, in different ways, to other structures seen near B5 IRS 1. Clump C appears to be associated with the CO outflow and may be related to a clump of emission seen in the blueshifted outflow material. Clump C also appears related to a region of enhanced brightness in the CCD image of the region. On the other hand, clumps A and B lie on a line which is perpendicular to the axis of the CO outflow and the average direction of the optical polarization of stars seen through the core. As will be discussed later, the direction of the elongated structure formed by clumps A and B also lies parallel to the direction of the large scale velocity gradient seen in the B5 core.

5.2. *Mass*

Table 3 gives estimates for the masses of the three HCN clumps. These values, which are in the range of 0.1–0.3 $M_\odot$, are probably uncertain by about a factor of 2. Also given in this table are the virial masses derived from the line width measured from the spectra averaged over each clump. These virial masses exceed the measured mass for each clump by a factor $\sim$6–10, using the observed line width at the clump position. If just the velocity range over which the clumps were identified is used, $\sim$0.5 km s^{-1}, the virial masses decrease by a factor of about 2. Integrating the emission over the whole central region 24" in radius, we find that the virial mass still exceeds the measured mass by a factor of about 2.5–5 (the virial mass is 2.6 $M_\odot$ as compared to a mass of 0.55–1 $M_\odot$ determined from the $F = 0 \rightarrow 1$ hyperfine component). Therefore it appears that the HCN clumps can not be bound by their own gravity, but it is possible that there might be enough mass in the central region that is not detected in the HCN to bind the clumps as a system.

From the submillimeter maps of the dust continuum emission Pendleton et al. (1990) estimate that the mean number density of the material within about 22" of IRS 1 is 2×10^5 cm^{-3}. This gives a mass of 2.5 $M_\odot$ which is very close to the mass necessary to bind the region of the HCN emission which is of a similar size. In addition to the gas and dust in the central region, there is the mass of IRS 1 which should be included when investigating whether the central region is bound. Models of the infrared spectrum of IRS 1 give an estimate of 0.3 $M_\odot$ (F. C. Adams, private communication) for the mass of the central star. However, its mass could be as high as 1.25 $M_\odot$, if the star is about to become optically visible on the stellar birthline described by Stahler (1983). This mass is close to the mass of 1.8 $M_\odot$ IRS 1 would have if it was a zero-age main-sequence star producing the observed luminosity.

Thus although the HCN clumps probably do not have sufficient mass to be individually bound, and for the region as a whole the virial mass of the HCN only exceeds the observed mass by a factor of 2.5–5, the mass derived from the submillimeter continuum observations plus the mass of the central star is very close to that which would be necessary to bind the HCN material. It therefore seems reasonable that the material currently seen in the circumstellar region of B5 IRS 1 is bound.

The various data on the B5 core can be used to investigate how the column density varies as a function of radius in the core. From 1.7 to 0.04 pc, a least-squares fit to H_2 column density, $N(r)$, versus size, r, in the log-log plane gives

$$N(r) \propto r^{-0.5 \pm 0.1} .$$

In addition to the HCN column density derived from the virial mass of the region close to B5 IRS 1 and the mean $C^{18}O$ column density from the map presented here, several other observations were used in this fit. For the largest scale, the column densities derived from the ^{12}CO and ^{13}CO luminosity mass from LWGB were used. In addition the ammonia data from Benson & Myers (1989), the size and mass estimate from the 360 μm data of Pendleton et al. (1990), and the column density derived from the virial mass plus observed core size of the CS data presented here were used. An estimate from the submillimeter continuum data of Pendleton et al. (1990) for the mass of the clump of material centered on IRS 1 was used in this fit. The dependence of the column density on radius indicates that the gas volume density within the core varies as

$$n(r) \propto r^{-1.5}$$

which is consistent with the form of density size relation derived for the sample of cores studied by Fuller (1989) and several other studies of core density profiles (Arquilla & Goldsmith 1985).

Models of cores such as those discussed by Shu, Adams, & Lizano (1987) propose that the inner regions of cores should be thermally supported and have density profiles approaching r^{-2}, whereas the outer regions which are magnetically supported have a r^{-1} density law. However, the data used to derive the column density–radius relation for B5 show no strong evidence for such a change in slope in the inner regions, although such a two-component fit is not inconsistent with the data.

In these models, the inner region of the cores which are infalling have density profiles which are proportional to $r^{-1.5}$, and hence column density $\propto r^{-0.5}$, similar to observed here in

B5. However, in the collapse models at any instant in time the mass in the central object (star plus disk) is approximately equal to the mass in the infalling envelope (Shu 1977). In the B5 core, this is clearly not the case over the range of sizes and densities covered by the ^{12}CO, ^{13}CO, CS, $C^{18}O$, and NH_3 maps. For all these observations the smaller scale structure always contains only a fraction of the larger scale mass. Only at the size of the HCN emission is it possible that the central star (plus any true circumstellar disk) contains a comparable amount of mass to the core material in its vicinity. This argues that the column density versus size relation seen for the core on the large scale does not reflect the fact that the core as a whole is in free-fall collapse. However, the similarity of HCN mass with the mass estimated for the central star suggests that perhaps the HCN material is part of the material infalling on to B5 IRS 1.

5.3. *Velocity Structure*

The $C^{18}O(J = 1 \rightarrow 0)$ and $CS(J = 2 \rightarrow 1)$ maps of B5 show velocity gradients of 0.60 ± 0.02 and 0.75 ± 0.03 km s^{-1} pc^{-1}, respectively. The direction of maximum gradient is $148° \pm 3°$ east of north for the $C^{18}O$ and $134° \pm 3°$ east of north for the CS. These directions are close to parallel to the direction of elongation of the clumps A and B and close to perpendicular to the axis of the CO outflow near IRS 1 and the average polarization vector for clouds seen through the B5 cloud (Joshi et al. 1985). Young et al. (1982) also found a velocity gradient in B5 of 1.6 km s^{-1} pc^{-1} in a parallel direction but on a size scale of ~ 1 pc. The velocity gradient in the ammonia data (Table 1) is consistent in both magnitude and direction with the gradients in the CS and $C^{18}O$. Assuming that the cloud is a uniform density sphere and the velocity gradients seen in CS and $C^{18}O$ are due to rotation, we find that the energy associated with these gradients to be 6×10^{42} and 10^{43} ergs, respectively (ignoring the effects of inclination to the line of sight) and less if the cloud is centrally condensed as it appears to be. Therefore, on the 0.5 pc scale of these maps the energy associated with this velocity gradient is not more than about 4% of the self-gravitational energy of the core and is thus unimportant for the structure of the core material.

On the smaller scale, the importance of rotation for the core material can be estimated from the HCN maps. Near IRS 1, the structure formed by clumps A and B appears flattened. The role of rotation in determining the structure of this material can be assessed from the velocity difference between these clumps. The line peak velocity difference between clumps A and B is a lower limit on the true rotational velocity of the A-B structure because all the material along the line of sight to the edge of the rotating structure contributes to the line profile at velocities closer to systemic velocity than the tangent point velocity. This skews the line peak position and causes the line profiles to be non-Gaussian. The contribution to the line profile from material at lower velocity than the tangent point material is exactly analogous to tangent point observations of H I in the Galaxy. The HCN data are of insufficient signal-to-noise ratio for this effect on the line shape to be seen. Nonetheless, the line peak velocity difference is a lower limit to the rotational velocity.

There is no evidence for a velocity difference between clumps A and B to a limit of 0.14 km s^{-1}. This corresponds to a limit on the velocity gradient of 4 km s^{-1} pc^{-1} and an energy of $\sim 4 \times 10^{41}$ ergs. However, to account for the potentially non-Gaussian line profiles discussed above, we estimate an upper limit on the rotational velocity gradient of ~ 6 km s^{-1} pc^{-1}. The energy associated with this rotational velocity still corresponds to only about 8% of the binding energy of the central region, adopting a mass of 2.6 $M_\odot$ from the HCN region virial mass. Thus rotation seems no more energetically important on the size scale of 0.04 pc, than on the much larger size scale traced by the CS and $C^{18}O$.

5.4. *Pervasive Clumps?*

Many authors have interpreted the emission from certain molecules as arising from dense, unresolved clumps within a cloud. Zhou et al. (1989) used this explanation to describe the CS emission from a number of dense cores, including B5. For B5, Zhou et al. derive a number density within the clumps of $10^{4.6}$ cm^{-3}, which is comparable to that of the HCN clumps near IRS 1. The size of the HCN clumps is also consistent with those claimed to be responsible for the CS emission. If the total mass of the $C^{18}O$ core around B5 IRS 1 is made up of these clumps, there would be ~ 170 clumps present in the $C^{18}O$ core. Is there any evidence for such structure?

If such clumps are present, they must survive for a time comparable to the lifetime of the core as a whole, or they must be continually formed. Indirect evidence from the statistics of young stars associated with ammonia cores suggest that an ammonia core exists for a few times its free fall time ($\sim 5 \times 10^5$ yr, for B5) before forming a young star (Beichman et al. 1986). If the $C^{18}O$ cores also survive for a few times their free-fall time, the B5 $C^{18}O$ core will probably exist for about 2×10^6 yr. A clump with a virial velocity dispersion of less than 0.2 km s^{-1}, the thermal dispersion of molecular hydrogen at 10 K, will disperse on order of the clump crossing time. Adopting the number density derived by Zhou et al. for the number density of the clumps, 4×10^4 cm^{-3}, this implies that clumps of radius less than 1.5×10^{17} cm (which is equal to the $C^{18}O$ beam radius) are unstable over the lifetime of the $C^{18}O$ core, and hence a regeneration mechanism must be postulated. Although for the current state of the B5 core it could perhaps be argued that the IRS 1 outflow might drive clump formation, there is little evidence that the outflow has significantly affected the bulk of the $C^{18}O$ core.

If clumps of radius 1.5×10^{17} cm and number density 4×10^4 cm^{-3} exist in B5, then to match the mass derived from the $C^{18}O$ observations about 170 clumps would have to be present. Each of these clumps would have a mean clump visual extinction of about 9 mag. If the clumps are randomly distributed within the core, each $C^{18}O$ beam should include about one clump and since a single clump fills the beam, the total column density per beam would be 9 mag, significantly higher than the observed mean of 6 mag. In addition if there is only one clump per beam, then the observed line width should reflect the clump line width. The observed mean line width of B5 in $C^{18}O$ is 0.85 km s^{-1}, which is clearly inconsistent with one clump per beam, if the clump internal velocity dispersion is sufficiently small that the clump does not disperse in the core lifetime. So it appears that the clumps cannot be pervasive and stable features of the $C^{18}O$ core. Either the fundamental structure of the core is not clumpy or the clumps are transient phenomena with lifetimes $\sim 10^5$ yr, less than one-tenth of the total expected $C^{18}O$ core lifetime, and a regeneration mechanism for the clumps must be postulated in order to maintain a clumpy structure within the core until the present time.

5.5. *Origin of the Circumstellar Structure of B5 IRS 1*

The properties of B5 derived from the observations discussed here are summarized in Table 4. The sizes given of the maps were measured from the area of the half-peak contour. Also given is the gravitational energy derived from each map. For the HCN clumps near B5 IRS 1, the binding energy given in the table is calculated assuming that the HCN region is gravitationally bound.

Structures similar to that formed by HCN clumps A and B have been called large circumstellar disks or toroids. This suggests that these structures reflect the original state of the circumstellar environment and hence are directly related to the star formation process. However, some caution must be exercised in applying this interpretation. Comparing the binding energy of the circumstellar material with the energy of the CO outflow, $\sim 3 \times 10^{43}$ ergs, which, using the dynamical age of the outflow, leads to an energy injection rate for the outflow of 2.4×10^{31} ergs s^{-1}, shows that the outflow currently has sufficient energy to disrupt the material in the local environment of IRS 1. So rather than directly reflecting the initial conditions for star formation, the structure we see today may be the result of star formation through the action of the outflow. For example, this means that the flattened structure observed in HCN could be the remains an initially spherical distribution of dense gas, some of which the outflow has now dispersed. More work is clearly needed to understand which of these two alternatives, original structure versus the effects of the outflow, is correct.

If the velocity gradients seen in the $C^{18}O$ and CS are due to rotation and this core were to collapse and there were no redistribution of angular momentum, then the material could infall until it reaches the radius at which it is in centrifugal balance. For the observed parameters of the $C^{18}O$ core, this size would be 2.7×10^{17} cm, which is only a factor of 2 larger than the observed size of the HCN region. However, the upper limit on the specific angular momentum in HCN clumps A and B is about 2% of that of the $C^{18}O$ material, which indicates that the HCN structure can not have resulted from the collapse of material similar to that currently seen in $C^{18}O$ if angular momentum was not redistributed during the collapse.

The HCN region has one very interesting property with respect to the models of core collapse. That is that the mass in the HCN is comparable to the mass in the central star. In the model of the collapse of singular isothermal spherical cores (Shu 1977), at any instant the mass of infalling material is equal to the mass in the central star plus disk. This is perhaps a suggestion that the HCN material is matter that is infalling onto IRS 1. One intriguing aspect of the data on this point is that toward HCN clumps A and B the $F = 0 \rightarrow 1$ hyperfine component, which, as discussed above, we believe traces the inner regions of the HCN material, has a slightly larger line width than the other two hyperfine components (Table 3). This may indicate unresolved motion of material in the inner regions of these clumps. A fuller investigation of this possibility must await higher resolution and higher signal-to-noise ratio data.

The morphology of the CO outflow and the optical arc nebula suggest a situation where the optical emission is light scattered off the wall of a cavity excavated by the CO outflow. If so, then the outflow is currently disrupting part of the dense core, similar to the situation of L43 (Mathieu et al. 1988). The outflow already has an energy comparable to the binding energy of the NH_3 clump associated with IRS 1, and only a few times less than the binding energy for the whole NH_3 core, so over the lifetime of IRS 1 as an embedded source with an outflow ($\sim$few $\times 10^5$ yr; Myers et al. 1987), the outflow will have several times the energy of the ammonia core and could therefore fully disrupt it. As is the case for the other cores, the fate of the $C^{18}O$ core is less clear (Fuller 1989).

In conclusion, of the three dense HCN clumps detected near B5 IRS 1, one (clump C) appears to be related to the outflow from IRS 1, or to the effects of the outflow on the surrounding material. This clump appears projected onto the blue lobe of the CO outflow close to the brightest region of an arc of optical emission which appears to mark the edge of the outflow. The other two clumps form an elongated structure near IRS 1 with the direction of elongation perpendicular to the axis of the outflow and parallel to the direction of the velocity gradient seen in the cloud on larger size scales. Although this structure has no measurable velocity gradient along its axis, it could be part of a large "circumstellar disk," similar to those claimed around other young stars (Beckwith et al. 1986) or a flattened region of infalling material. However, in view of the energetics of the outflow associated with IRS 1, it is possible that the current nature of this structure is the result of the action of the outflow.

6. CONCLUSIONS

1. The B5 dense core has been mapped in $C^{18}O$ and CS and these two tracers both reveal a similar structure for the core. The core appears primarily elongated N-S with perhaps some suggestion of slightly convex appearance. These maps are quite similar in overall shape to both the existing submillimeter continuum maps and the NH_3 map of this core, although the size of the core is different in each tracer.

2. The CO outflow from B5 IRS 1 has a total extent of about 0.5 pc in a direction about 65° east of north, close to perpendicular to the direction of the $C^{18}O$ and CS velocity gradient. The outflow is very well collimated with an axial ratio of about 3:1. The direction of the axis of the CO outflow is close to parallel to the major axis of ^{12}CO map of B5. An arc of optical emission surrounds the outer edge of the blueshifted CO near B5 IRS 1.

3. High-resolution maps of HCN show three clumps of material near IRS 1. One appears associated with the outflow and optical emission arc, whereas the other two appear to form an elongated structure close to IRS 1. The direction of elongation of this structure is in a direction which is perpendicular to both the major axis of the outflow near IRS 1 and the axis of the velocity gradient seen in the CS and $C^{18}O$ maps. This elongated structure is similar to structures which have been previously described as large circumstellar disks or toroids. However, for B5 it is unclear whether this structure really reflects the original distribution of material near IRS 1. The outflow from B5 IRS 1 is sufficiently energetic and massive that the observed clumps could be remnant material or material swept-up by the outflow and not reflect the original structure of the circumstellar environment of IRS 1.

4. The mass of the HCN region is comparable to the mass of the central young star which is suggestive that the HCN material is matter infalling on to the central star.

5. There is no evidence for an ordered velocity field in the HCN near IRS 1. The upper limit this places on the rotation suggests that although rotation could represent a slightly larger faction of the core gravitation energy at $\sim 10^{17}$ cm from

IRS 1 than on the scale of the velocity gradient seen in the $C^{18}O$ and CS, $\sim 10^{18}$ cm, even at the small size scale, rotation is not important for the structure of the material. The specific angular momentum in the HCN structure is less than about 2% of the specific angular momentum of the $C^{18}O$ material.

6. The HCN spectra, when analyzed in the light of the other data on the core, can be explained in terms of a model where foreground absorption plays an important role in determining the observed spectra. This demonstrates that when interpreting observations of the internal structure of cores, the internal structure should not be treated in isolation from the rest of the core material.

7. Analysis of the data on B5 from sizes of 1.7 down to 0.04 pc indicates that the volume density of the material in the core varies as $r^{-1.5}$ on average.

G. A. F. wishes to acknowledge the support of NSF AST87-14721 grant to the Radio Astronomy Laboratory, U.C. Berkeley, the Smithsonian Pre-Doctoral Fellowship Program, and a Center for Astrophysics Fellowship. We thank M. C. H. Wright for helpful discussions about the acquisition and reduction of the BIMA data. FCRAO is supported in part by NSF grant AST88-15406. W. D. L. acknowledges the hospitality of the Université de Grenoble during part of this work.

REFERENCES

Arquilla, R., & Goldsmith, P. F. 1985, ApJ, 297, 436
Bachiller, R., & Cernicharo, J. 1986, A&A, 166, 283
Beckwith, S., Sargent, A. I., Scoville, N. Z., Masson, C. R., Zuckerman, B., & Phillips, T. G. 1986, ApJ, 309, 755
Beichman, C. A., Myers, P. C., Emerson, J. P., Harris, S., Mathieu, R., Benson, P. J., & Jennings, R. E. 1986, ApJ, 307, 337
Beichman, C. A., et al. 1984, ApJ, 278, L45
Benson, P. J. 1983, Ph.D. thesis, Department of Physics, M.I.T.
Benson, P. J., & Myers, P. C. 1989, ApJS, 71, 89
Barnes, C. 1979, A&A, 73, 67
Bohlin, R. C., Savage, B. D., & Drake, J. F. 1978, ApJ, 224, 132
Cernicharo, J., & Bachiller, R. 1984, A&AS, 58, 327
Cernicharo, J., Castets, A., Duvert, G., & Guilloteau, S. 1984, A&A, 139, L13
Fuller, G. A. 1989, Ph.D. thesis, Astronomy Department, University of California, Berkeley
Fuller, G. A., & Myers, P. C. 1991, in preparation
Goldsmith, P. F., Langer, W. D., & Wilson, R. W. 1986, ApJ, 303, L11 (GLW)
Goldsmith, P. F., Snell, R. L., Hemeon-Heyer, M., & Langer, W. D. 1984, ApJ, 286, 599
Gottlieb, C. A., Lada, C. J., Webster Gottlieb, E., Lilley, A. E., & Litvak, M. M. 1975, ApJ, 202, 655
Green, S., & Thaddeus, P. 1974, ApJ, 191, 653
Guilloteau, S., & Baudry, A. 1981, A&A, 97, 213
Hawkins, I., & Jura, M. 1987, ApJ, 317, 926
Herbig, G. H., & Jones, B. F. 1983, AJ, 88, 1040
Heyer, M. H., Ladd, E. F., Myers, P. C., & Campbell, B. 1990, AJ, 99, 1585
Irvine, W. M., Goldsmith, P. F., & Hjalmarson, A. 1987, in Interstellar Processes, ed. D. J. Hollenbach & H. A. Thronson (Dordrecht: Reidel), 561
Irvine, W. M., & Schloerb, F. P. 1984, ApJ, 282, 516
Joshi, U. C., Kulkarni, P. V., Bhatt, H. C., Kulshrestha, A. K., & Deshpande, M. R. 1985, MNRAS, 215, 275
Langer, W. D., & Graedel, T. E. 1989, ApJS, 69, 241
Langer, W. D., & Penzias, A. A. 1990, ApJ, 357, 477
Langer, W. D., Wilson, R. W., Goldsmith, P. F., & Beichman, C. A. 1989, ApJ, 337, 355 (LWGB)
Mathieu, R. D., Benson, P. J., Fuller, G. A., Myers, P. C., & Schild, R. E. 1988, ApJ, 330, 385
Monteiro, T. S., & Stutzki, J. 1986, MNRAS, 221, 33P
Myers, P. C., & Benson, P. J. 1983, ApJ, 266, 309
Myers, P. C., Fuller, G. A., Goodman, A. A., & Benson, P. J. 1991, ApJ, in press
Myers, P. C., Fuller, G. A., Mathieu, R. D., Beichman, C. A., Benson, P. J., Schild, R. E., & Emerson, J. P. 1987, ApJ, 319, 340
Myers, P. C., Linke, R. A., & Benson, P. J. 1983, ApJ, 264, 517
Pendleton, Y., Davidson, J., Casey, S., Harper, A., Pernic, R., & Myers, P. C. 1990, in Submillimetre Astronomy, ed. G. D. Watt & A. S. Webster (Dordrecht: Kluwer), 189
Shu, F. H. 1977, ApJ, 214, 488
Shu, F. H., Adams, F. C., & Lizano, S. 1987, ARA&A, 25, 23
Stahler, S. W. 1983, ApJ, 274, 822
Swade, D. A. 1989, ApJ, 345, 828
Vogel, S. N., Wright, M. C. H., Plambeck, R. L., & Welch, W. J. 1984, ApJ, 283, 655
Walmsley, C. M., Churchwell, E., Nash, A., & Fitzpatrick, E. 1982, ApJ, 258, L75
Wannier, P. G., Penzias, A. A., & Jenkins, E. B. 1982, ApJ, 254, 100
Wilson, R. W., Langer, W. D., & Goldsmith, P. F. 1981, ApJ, 243, L47
Young, J. S., Goldsmith, P. F., Langer, W. D., Wilson, R. W., & Carlson, E. R. 1982, ApJ, 261, 513
Zhou, S., Wu, Y., Evans, N. J., Fuller, G. A., & Myers, P. C. 1989, ApJ, 346, 168